Article

The Effect of Diameter and Position of Transverse Cylindrical Vortex Generators on Heat Transfer Improvement in a Wavy Channel

Stanislav Kotšmíd [ID] and Zuzana Brodnianská *[ID]

Faculty of Technology, Technical University in Zvolen, Studentska 26, 960 01 Zvolen, Slovakia
* Correspondence: zuzana.brodnianska@tuzvo.sk

Abstract: The present study investigates the effect of outer diameter (10 mm and 15 mm) and 5 positions of cylindrical vortex generators (CVGs) installed to the wavy channel in order to improve heat transfer parameters in conjunction with low-pressure drops. The wavy channels with and without CVGs are compared in terms of the local heat transfer coefficient, mean Nusselt number, Colburn factor, friction, and thermal performance for Re in the range of 857 to 8001. Furthermore, the effect of the cooling air flow direction (forward and backward) is assessed. Inserting the CVGs to the channel causes the enhancement of Nusselt numbers and Colburn factors for all CVGs positions and Re in comparison with the channels without CVGs. The maximum thermal performance factor $TPF_B = 0.8229$ was achieved for the channel with CVGs position '5' and 15 mm diameter, backward air flow, and $Re = 1677$. The backward air flow is more efficient compared with forward air flow since the cooling air gets into the valleys to a greater extent, and thus, better mixing of the fluid occurs. The numerical investigation, conducted with Ansys Fluent software, is compared with the experimental one acquired by holographic interferometry at good agreement of the local heat transfer coefficients. Finally, new correlating equations for the mean Nusselt number were created.

Keywords: wavy channel; cylindrical vortex generator; heat transfer; thermal performance; numerical simulation

MSC: 65D10; 76M12; 80M12

1. Introduction

Plenty of experimental and numerical studies have been devoted to the enhanced heat transfer of rectangular corrugated channels that are widely employed as heat exchangers, recovery units, electronic devices, solar air heater, and different heaters and coolers in the field of energy, mechanical and chemical engineering, aerospace technology, laser equipment and automotive. The corrugation of heat exchange surfaces leads to the flow deviation and acceleration adjacent to the wavy protrusions, which results in intensifying the convective rate of heat transfer [1]. In many studies, the insertion of various vortex generators (VGs) into the flowing medium has been confirmed as effective in terms of thermal performance improvement; however, certain pressure losses always appear there.

The advantage of wavy channels is the creation of recirculation or/and swirl flows in the corrugation valleys. The onset and growth of recirculation zones promote the mixing of air in the boundary layer. Therefore, the wavy surface has a significant effect on the enhancement of heat transfer [2]. Naphon [2] experimentally studied the channel with height of 12.5 mm and V inline corrugated lower and upper heated surfaces with the corrugation tile angle of 20°, 40°, and 60° for heat flux $q = 0.5$–1.2 kW/m^2 and $Re = 500$–1400. The Nusselt numbers at higher corrugated tile angles were higher than those at lower ones. Consequently, Naphon [3] also studied the channel height of 20 and 25 mm with the length of channel 300 mm for staggered arrangement and Re in the range

of 2000–9000. The heat transfer and pressure drop for the corrugated channel are 3.51 and 1.96 times higher than those for the smooth channel. Three wavy channels applied as solar air heaters for the mass flow rate in the range from 0.01 kg/s to 0.04 kg/s were experimentally studied by Singh et al. [4]. The maximum thermal performance was achieved for mass flow rate of 0.04 kg/s. The thermal performance increased from 47% to 66% with increased mass flow rate from 0.01 kg/s to 0.04 kg/s, respectively. The solar air heaters with a different shape of VGs were explored experimentally and numerically by several authors. Conical VGs in a staggered arrangement used by Bezbaruah et al. [5] achieved 257% enhancement in thermal performance. According to Silva et al. [6], the VG shape and angle of attack affect the heat transfer more than Re number. In the paper by Zhao [7], the V-shaped ribs and the delta winglet VG pair were studied to investigate the mixing effect in the solar air heater channel. The delta-winglet VGs combined with the 60° V-shaped ribs achieved the enhanced heat transfer by 39.4% compared with the only delta-winglet VG case. The combination of a sinusoidal wavy channel and VGs brought an increase in terms of thermal performance factor in several studies. Caliskan et al. [8] achieved the improvement of 2.2 times due to VG, sinusoidal structure, and punched hole. To mix the flow and enhance the convection, Nassab et al. [9] attached the inclined thin elastic porous winglet on the heated wall as the VG in the solar air heater. The porous VG significantly improved the outlet bulk temperature difference up to 500%. Particle image velocimetry (PIV) was used by Kurtulmus et al. [10] to investigate the flow physics in the wavy converging-diverging channel for Re in the range of 4×10^3 to 1×10^4. They conducted the numerical simulations to confirm the experimental results for the same parameters. The shear stress transport $k\text{-}\omega$ turbulence model was used to perform numerical analyses. The highest TPF = 1.46 was obtained for the ratio of maximum channel height to minimum channel height of 0.5 and $Re = 4 \times 10^3$.

Enhancing the efficiency of channel/microchannel heat exchangers is important from the standpoint of the cooled electronic/microelectronic component proper functioning. Liu et al. [11] achieved the critical Re numbers from 600 to 700 using the longitudinal VGs in a microchannel and improved the heat transfer performance (9–21% higher for the laminar flow and 39–90% for the turbulent flow). Due to this, the pressure drops increase as well (34–83% for the laminar flow and 61–169% for the turbulent flow). Moreover, the empirical correlations for Nusselt numbers and friction factors were developed. Chen et al. [12] presented an increase in heat transfer performance by 12.3–73.8% and 3.4–45.4% for the microchannels with longitudinal VGs and the aspect ratios of 0.0667 and 0.25, respectively, while the pressure drops were increased by 40.3–158.6% and 6.5–47.7%. The VGs help to achieve the critical Re numbers lower than 1000, which is below the generally accepted value of 2300. A single-phase laminar flow in the rectangular microchannel equipped with longitudinal VGs was numerically studied by Ebrahimi et al. [13]. When comparing the channel with longitudinal VGs and the smooth microchannel for Re in the range of 100 to 1100, the increase of 2–25% in the mean Nusselt number was observed for the former one. Higher Re numbers caused higher heat transfer enhancement; however, VGs caused higher-pressure drops. Raihan et al. [14] placed the CVGs to the heat sinks where the lowest thermal resistance was achieved for the VGs at the front of the minichannels with the radius 300 μm and no distance between them and found that pressure drop increased with a larger VG radius. To increase heat transfer, the simultaneous use of transverse VGs and porous media in the microchannel was investigated by Moosavi et al. [15]. The convective heat transfer coefficient increased with the height and number of VGs. There was an enhancement of 260–1200% in terms of Re number in the range of 125 to 1000. The VGs caused better overall performance in the microchannel than the porous medium. Compared with the empty microchannel, the heat transfer coefficient is 2.6 times higher when using 8 VGs with 12.5% of the channel height. Amini and Habibi [16] used the flexible splitters for enhanced heat transfer capability and higher hydrothermal performance of heat sink. The flexible splitters achieved better heat transfer capability and higher hydrothermal performance compared with the rigid ones. In comparison with

the channel without splitters, the flexible splitters achieved 10% less total hydrothermal efficiency and 190% higher rejected heat.

Al-Asadi et al. [17] numerically explored the cylindrical vortex generators (CVGs) of radii up to 400 μm with a half-circle and quarter-circle cross section in a microchannel in terms of thermal resistance, pressure drop, and performance evaluation criteria index (pressure drop vs. thermal resistance). The uniform heat flux and *Re* number in the range of 100 to 2300 represented the conditions for microelectronic cooling. The research confirmed the significant potential of using VGs. Based on the performance evaluation criteria index, small-radius centered VGs offer a good potential for the efficiency improvement at lower *Re* number. Subsequently, Al-Asadi et al. [18] studied various gaps along the CVGs' length placed transversely over the microchannel span to reduce the pressure drop and enhance heat transfer performance. The gaps between each end of the VGs and the channel side wall offer enhanced performance. Cylinders of a circular, square, or possibly oval shape are inserted into the rectangular channels for the purpose of breaking up the air and creating vortices. Leu et al. [19] inserted the inclined block-shape VGs behind the tubes of a plate-fin and tube heat exchanger. The VGs' span angle of 45° provides the best heat transfer augmentation since the longitudinal vortices are generated and the heat transfer performance in the wake regions is improved. The adiabatic circular cylinder in the uniformly heated mini-channel was numerically investigated by Cheraghi et al. [20]. It was found that the maximum heat transfer enhancement from channel walls is achieved when the cylinder is placed in the middle of the channel. An important conclusion is that the displacement of cylinder towards the bottom wall leads to the suppression of the vortex shedding, establishment of a steady flow, and reduction of both wall heat transfer and pressure drop. The improvement in thermal performance of a rectangular channel with small-scale CVGs was achieved by Wang [21] where the circular cylinder was located in a fully developed turbulent boundary layer of a rectangular channel. The interaction between the cylinder wake and the wall boundary layer altered the flow structure of the turbulent boundary layer. Consequently, Wang [22] used the small-scale slit-vent circular cylinder in the mentioned channel. When the gap ratio (distance from the cylinder to channel bottom/cylinder diameter) was more than 2, the overall thermal performance of a rectangular channel with the slit-vent cylinder was improved. Han et al. [23] inserted a half-cylinder as the VG to the rectangular channel; consequently, the effects of the height, length, and spacing of the VGs were studied by Han et al. [24].

The channel fitted with a circular cylinder was researched experimentally by Vyas [25]. The interferometry method showed the effect of the cylinder in generating the flow instabilities and alterations in the thermal boundary layer along the heated channel wall. Moreover, the vortex shedding behind the cylinder was captured and a gradual increase in the vortex shedding frequency was observed with increasing *Re* number. Dey [26] varied the axial and transverse location of an adiabatic square cylinder in the channel to analyze the effect of the parameters on the wall heat transfer performance and the channel flow characteristics. Particle swarm optimization was used to find out that the ratio $L_2/D = 33$ and $H/D = 10$ can provide the maximum thermal performance ($\eta = 1.063$) when the cylinder is placed at $s/D = 5$ and $H/D = 3$ for *Re* = 100. The effect of the round, oval, and diamond shape of the pins in combination with the VGs in a microchannel on the heat transfer enhancement was investigated in the paper by Wang [27]. The VGs intensified the fluid mixing and increased the secondary flow by 30%. For the purpose of increasing the average heat transfer, the punched delta winglet pair as a longitudinal VG was used by Wu [28]. The average Nusselt number increased with the attack angle of the delta winglet pair. Zhang [29] studied the heat transfer performances and flow characteristics of VGs in the high aspect ratio rectangular ribbed channel. Liquid crystal thermography and CFD simulations with the SST k-ω model in a transition state were used for the experimentally and numerically studies. The flow characteristics revealed that longitudinal VGs generated the vortices to disturb the boundary layers, which enhanced the flow mixing and augmented the heat transfer performance. In the paper by Ibrahim [30], the winglet VGs (delta

and rectangular) in the bank of oval tubes were used. On the basis of the experimental results, it was found that the delta winglets give the best performance in the single-phase and two-phase flow tube bank of oval tubes.

In this study, the examined asymmetric wavy geometry of the heated channel is the novel geometry, and in combination with the appropriate placement and outer diameter of CVGs, it improves heat transfer processes due to the direction and pressing of cooling air into the valleys and the creation of recirculation zones. The direction of inlet cooling air also plays an important role in heat transfer intensification due to different flow characteristics in the channel. In the previous literature, the channels with symmetric wavy protrusions were investigated mainly that did not achieve such a significant improvement in heat transfer characteristics. This fact motivated us to design and investigate a new geometric shape of heat exchange surfaces. Moreover, with the addition of CVGs, the possibilities of further increases in thermal performance have been expanded.

2. Numerical Background

2.1. Physical Model

The geometric dimensions of the examined configurations are shown in Figure 1. The length of 400 mm, the height of 40 mm, spacing between protrusions peaks of 40 mm, and the shape of the wavy channel protrusions were identical for all configurations. The cylindrical vortex generators (CVGs) with the diameter of 10 and 15 mm were inserted to the wavy channel in five different horizontal positions (Figure 1b,c). Overall, eight CVGs were centered relative to the channel height. The air flowed forward (air inlet A) and backward (air inlet B) through the channel for all examined configurations. The wavy channels with the CVGs diameter of 10 mm (Figure 1b) and 15 mm (Figure 1c) were compared with the wavy channel without CVGs (Figure 1a). The surface temperature of wavy surfaces was kept to T_s = 318.15 K while the air flow through the wavy channel was changed in the range of 5 to 50 m^3/h.
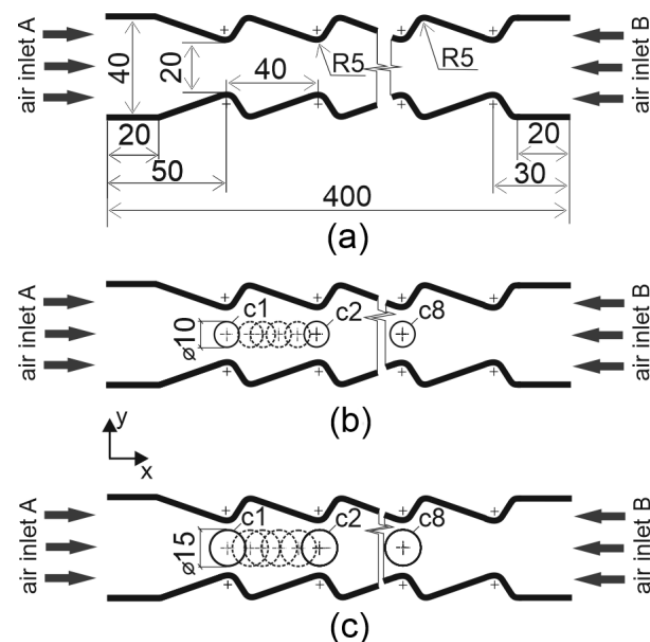

Figure 1. Geometric dimensions of the examined configurations (**a**) wavy channel A (WCA) and wavy channel B (WCB), (**b**) wavy channel A with CVGs diameter of 10 mm (WCCA10) and wavy channel B with CVGs diameter of 10 mm (WCCB10), (**c**) wavy channel A with CVGs diameter of 15 mm (WCCA15) and wavy channel B with CVGs diameter of 15 mm (WCCB15).

The configurations of the examined channels are shown in Table 1. For the sake of clarity, the investigated configurations are defined by the abbreviations. The wavy channel

with forward air flow (WCA) and the wavy channel with backward air flow (WCB) do not include the CVGs. In the wavy channels with the CVG diameter of 10 mm (WCCA10) and 15 mm (WCCA15) with forward air flow, the CVGs' horizontal position in the range of $x_0/s = 0$ to $x_4/s = 0.79$ was considered. The same conditions were set for backward air flow (WCCB10, WCCB15).

Table 1. Examined configurations and positions of the cylindrical vortex generators (CVGs).

Configuration	Q (m³/h)	Cylindrical Vortex Generators
Wavy channel A (WCA)		none
Wavy channel B (WCB)		none
Wavy channel A with CVGs ø 10 mm (WCCA10)	5, 10, 15, 20, 30, 40, 50	horizontal change position: $x_0/s = 0$, $x_1/s = 0.27$, $x_2/s = 0.38$, $x_3/s = 0.58$, $x_4/s = 0.79$
Wavy channel A with CVGs ø 15 mm (WCCA15)		
Wavy channel B with CVGs ø 10 mm (WCCB10)		
Wavy channel B with CVGs ø 15 mm (WCCB15)		

2.2. Data Reduction

The local heat transfer coefficients from numerical simulations are calculated by Sui [31]:

$$h_x = \frac{q_x}{\frac{\left(T_s - T_{a,in,m}\right) - \left(T_s - T_{a,out,m}\right)}{\ln\left[\frac{\left(T_s - T_{a,in,m}\right)}{\left(T_s - T_{a,out,m}\right)}\right]}} \tag{1}$$

The mean Nusselt number of the whole channel is defined as [32]:

$$Nu_m = \frac{h_m \cdot D_{hyd}}{k_a} \tag{2}$$

Hence, the hydraulic diameter was defined as $D_{hyd} = (2 \cdot W \cdot H)/(W + H)$ [33]. The mean heat transfer coefficient for the whole channel is defined as [32]:

$$h_m = \frac{\int_0^L (h_{x,l} + h_{x,u}) dx}{2L} \tag{3}$$

where L is the contour length of wavy surfaces in the test section.

The Colburn factor j and friction factor f of the whole channel are defined as [34]:

$$j = \frac{Nu_m}{Re \cdot Pr^{\frac{1}{3}}} \tag{4}$$

and [35]:

$$f = \frac{\Delta p}{\frac{L_2}{D_{hyd}} \cdot \frac{\rho_a \cdot v_{a,m}^2}{2}} \tag{5}$$

The thermal performance factor of the wavy channel with CVGs vs. wavy channel without CVGs for forward air flow (air inlet A) is defined as [5]:

$$TPF_A = \left(\frac{Nu_{WCCA}}{Nu_{WCA}}\right)\left(\frac{f_{WCCA}}{f_{WCA}}\right)^{-\frac{1}{3}} \tag{6}$$

while for backward air flow (air inlet B), it is defined as [5]:

$$TPF_B = \left(\frac{Nu_{WCCB}}{Nu_{WCB}}\right)\left(\frac{f_{WCCB}}{f_{WCB}}\right)^{-\frac{1}{3}} \tag{7}$$

2.3. Boundary Conditions

A preliminary study of the mesh grid size was carried out where quadrilateral elements were used. Overall, five different numbers of elements were created in the wall adjacent area, and the average heat transfer coefficient for the channel was being evaluated. Each mesh variant has a different number and bias of elements in perpendicular direction to the wall. On the basis of the study, the mesh with 2970 elements in the wall adjacent area was sufficient from the accuracy point of view. When refining the domain, maximum 0.4% improvement could be achieved. The average element height on the wall 0.082 mm continuously increased to 0.162 mm in the middle of the channel. Furthermore, the y^+ values were controlled as another quality criterion. Considering the element quality (aspect ratio, angles, etc.), the element widths were appropriately adjusted. The blue line of the mesh dependency test represents the change in the mean heat transfer coefficient h_m depending on the number of elements (Figure 2). The percentage discrepancy of h_m between two consecutive numbers is represented by the green line. The maximum limit of 2% for a sufficient number of elements is represented by the red dotted line.
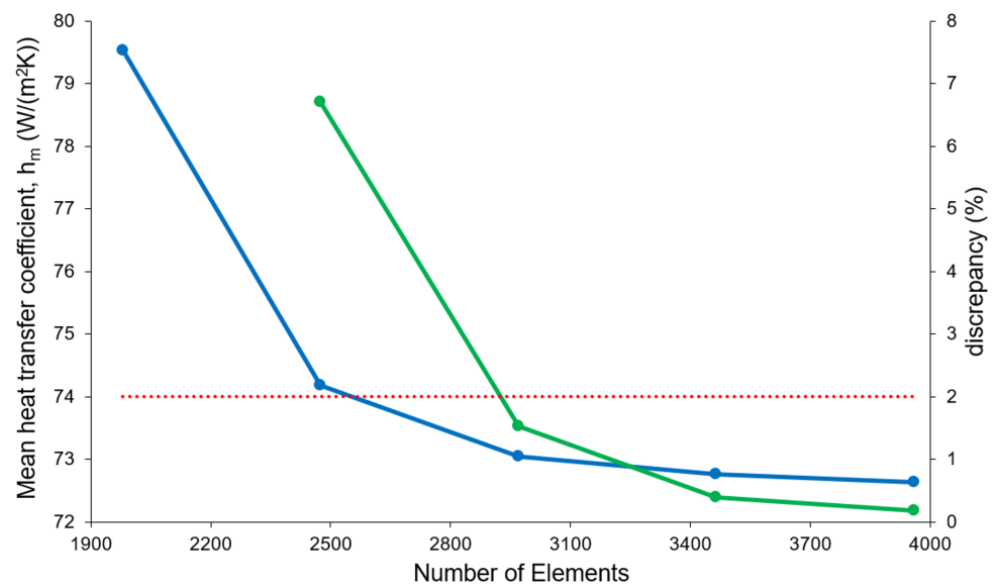

Figure 2. Mesh dependency test.

The governing equations of mass, momentum, and energy conservation were solved by the Ansys Fluent software in the following form [18]:

Continuity equation:

$$\nabla \cdot (\rho \mathbf{v}) = 0 \tag{8}$$

Momentum equation:

$$\nabla \cdot \left(\rho \mathbf{v}\mathbf{v}^T\right) = -\nabla p + \nabla \cdot \left\{\mu\left[\nabla\mathbf{v} + (\nabla\mathbf{v})^T - \frac{2}{3}(\nabla\cdot\mathbf{v})\mathbf{I}\right]\right\} + \rho\mathbf{g} \tag{9}$$

Energy equation:

$$\nabla \cdot \left(\rho c_p \mathbf{v}T\right) = \nabla \cdot (k\nabla T) \tag{10}$$

The turbulent flow was solved by the k-ω SST model using the incompressible ideal gas density. The pressure–velocity coupling was handled by the coupled scheme with the

pseudo transient formulation while the second–order upwind schemes were used as a spatial discretization. The solution was considered to be fully converged when the residuals of continuity, velocity, energy, k, and ω reached the criterion 10^{-6}.

The flow is considered to be steady two-dimensional with the air variable properties as follows:

$$k(T) = -2.48 \cdot 10^{-8} T^2 + 8.92 \cdot 10^{-5} T + 1.12 \cdot 10^{-3} \tag{11}$$

$$\mu(T) = -3.76 \cdot 10^{-11} T^2 + 6.95 \cdot 10^{-8} T + 1.12 \cdot 10^{-6} \tag{12}$$

$$c_p(T) = 3.34 \cdot 10^{-4} T^2 - 0.156 T + 1023.53 \tag{13}$$

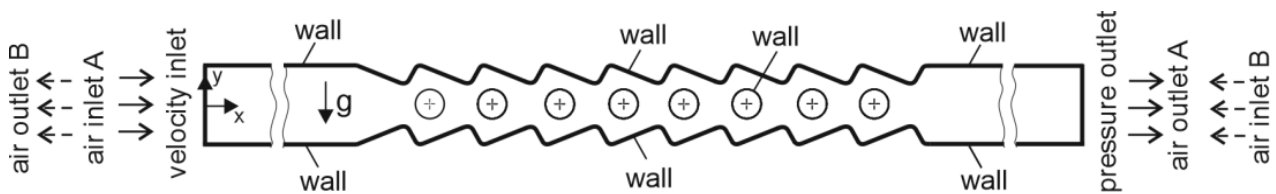The boundary conditions according to Figure 3 are described as follows:

Figure 3. Boundary conditions for forward and backward air flow in the wavy channel.

- velocity inlet—air inlet A, B:

$$v_x = v_{in,a} = const., \qquad v_y = 0, \qquad T = T_{in,a} = const. \tag{14}$$

- pressure outlet—air outlet A, B:

$$\frac{\partial v_x}{\partial x} = \frac{\partial v_y}{\partial x} = \frac{\partial T}{\partial x} = 0 \tag{15}$$

- wall—tubes, inlet and outlet section:

$$v_x = v_y = 0, \qquad \frac{\partial T}{\partial n} = 0 \tag{16}$$

- wall—test section:

$$v_x = v_y = 0, \qquad T = T_s = const. \tag{17}$$

3. Experimental Validation

The holographic interferometry method was used to obtain the local heat transfer coefficients for the wavy channel without CVGs and forward air flow (WCA) and the wavy channel with CVGs of 15 mm diameter for forward air flow (WCCA15) [32,36]. Two coherent waves interacted with each other where one wave deformed when passing through the temperature field and the other one passed outside. The variant of Mach–Zehnder interferometer was used to visualize the temperature fields in the vicinity of wavy protrusions. The resulting interference fringes on the interferograms represented the isotherms in the vicinity of the heated wavy surfaces. The experimental local heat transfer coefficients h_{xexp} for the WCA and WCCA15 at the local sections '1' to '5' were compared with the local heat transfer coefficients h_{xnum} obtained by numerical simulations (Figure 4). The discrepancies in the local heat transfer coefficient between the numerical and experimental results for all local sections were below 19.67%.
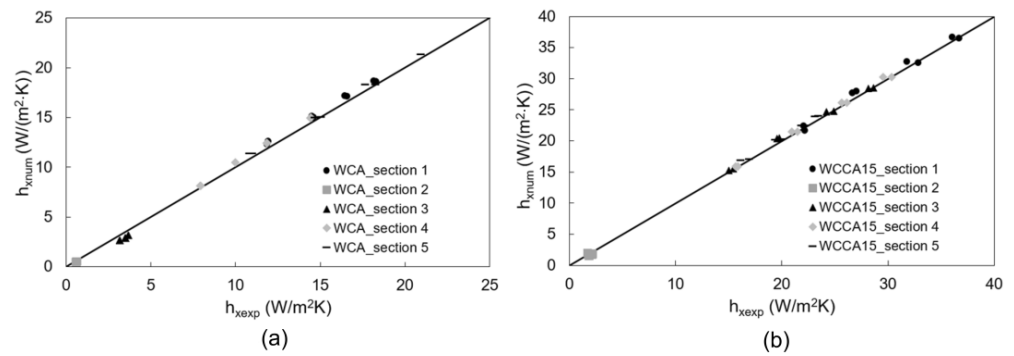
Figure 4. Comparison between the experimental and numerical local heat transfer coefficients for $H = 40$ mm, $T_s = 318.15$ K, $Q = 5$–20 m^3/h, (**a**) wavy channel without CVGs, (**b**) wavy channel with CVGs of 15 mm diameter.

4. Results and Discussion

The courses of the mean Nusselt numbers Nu_m for all investigated wavy channels are shown in Figure 8. An increase of Nu_m with Re was confirmed for all investigated configurations, while the size of the recirculation zone and the vortex strength in the valleys formed an increase in heat transfer. When evaluating the wavy channels without CVGs, the values of Nu_m for WCB were higher in the range of 1.28% to 5.09% compared with WCA for $Q = 10$–50 m^3/h. On the contrary, the WCA achieved higher Nu_m by 4.78% compared with the WCB for $Q = 5$ m^3/h. The Nu_m values increased with Re in the range of 11.06 to 58.48 and 10.53 to 61.16 for the configuration WCA and WCB, respectively.

The local heat transfer coefficients h_x along the lower and upper heated surfaces for the WCA and WCB configurations and $Q = 50$ m^3/h are compared in Figure 5. It is shown that the distribution of h_x did not change significantly. The maximum h_x was achieved on the 2nd protrusion of the WCA at the local section of 0.288 m ($h_x = 65.42$ W/(m^2·K) and on the 8th protrusion of the WCB at the local section of 0.532 m ($h_x = 89.70$ W/(m^2·K). The fundamental difference between the compared configurations is that the peaks of WCB protrusions gradually increase along the channel; on the other hand, the peaks of WCA protrusions gradually decrease. This fact has a significant effect on the overall heat transfer through the wavy channel. It was found that the backward air flow improved the local and mean heat transfer parameters compared with the forward one. The backward air flow changes the flow characteristics in the channel, i.e., the distribution of velocity and pressure parameters. The flowing air is slowed down more when hitting the peaks of the protrusions and does not flow smoothly in the vicinity of the protrusions as in the case of forward air flow. The better mixing of air in the valleys leads to an increase in h_x.
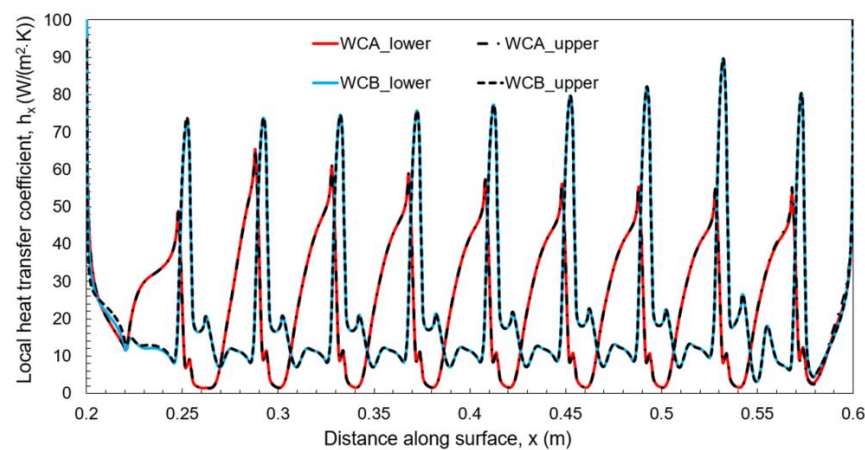

Figure 5. The comparison of the local heat transfer coefficients along the lower and upper heated surfaces of WCA and WCB configurations for $Q = 50$ m^3/h.

The distribution of the temperature fields along the WCA and WCB length for $Q = 50$ m^3/h are shown in Figures 6 and 7. The detailed distribution of the temperature fields and velocity vectors in the vicinity of the 2nd protrusion (WCA) and the 8th protrusion (WCB) is shown in Figure 6b,c and Figure 7b,c, respectively. In the both cases, the thermal boundary layer thickness increases with the channel length. For the WCB configuration, the cooling air causes better mixing in valleys, which leads to more efficient heat transfer in the valleys and subsequently higher h_x compared with the WCA configuration (Figures 5–7). For the WCA configuration, the minimum $h_x = 1.39$ W/(m^2·K) and maximum $h_x = 65.42$ W/(m^2·K) are achieved on the 2nd protrusion at the local sections 0.261 m and 0.288 m (Figure 6b), respectively. For the other protrusions, there are minimum h_x values in the valleys and maximum h_x values at the leading edge before reaching the protrusion top; however, h_x gradually decreases with the channel length. The effect of the air recirculation appears in the valleys while two recirculation zones are formed for the WCA configuration (Figure 6c). In the valleys, the air flow slows down and its recirculation occurs there (Figures 6c and 7c). For the WCB configuration, the minimum $h_x = 3.11$ W/(m^2·K) and maximum $h_x = 89.70$ W/(m^2·K) are achieved on the 8th protrusion at the local sections 0.549 m and 0.532 m (Figure 7b), respectively. Only one recirculation zone is formed in the valleys; however, the flow rate is intensive enough to improve heat transfer there (Figure 7c). More intense flow of cooling air in the valleys leads to an increase in both local and mean heat transfer parameters for the WCB configuration.

When comparing the WCA, WCB, and wavy channels with CVGs (10 mm, 15 mm), the first mentioned configuration achieved lower Nu_m for all investigated CVGs positions (Figure 8). It was found that Nu_m decreases with CVGs position (1 to 4) for all wavy channels; however, there is an increase at the position '5'. The maximum Nu_m in the range of 40.21 to 163.74 ($Re = 857$ to 6383) was achieved for the configuration of WCCA15 and CVGs position '1' (Figure 8a). On the other hand, the maximum $Nu_m = 196.00$ was obtained for the configuration of WCCB15 (position '1') and $Re = 8000$. The Nu_m increased 3.35 times for the WCCA15 (position '1') compared with the WCA for the maximum flow rate of 50 m^3/h. When changing the CVGs positions from '1' to '4', the difference between Nu_m values decreased while Nu_m for the WCCA15 (position '4') was only 1.81 times higher compared with the WCA. On the contrary, the difference between Nu_m of the mentioned configurations increased for the position '5' (2.31 times in favor of the WCCA15). The Prandtl number of the air inlet temperature 296.15 K represents the value of 0.729 for all examined configurations.
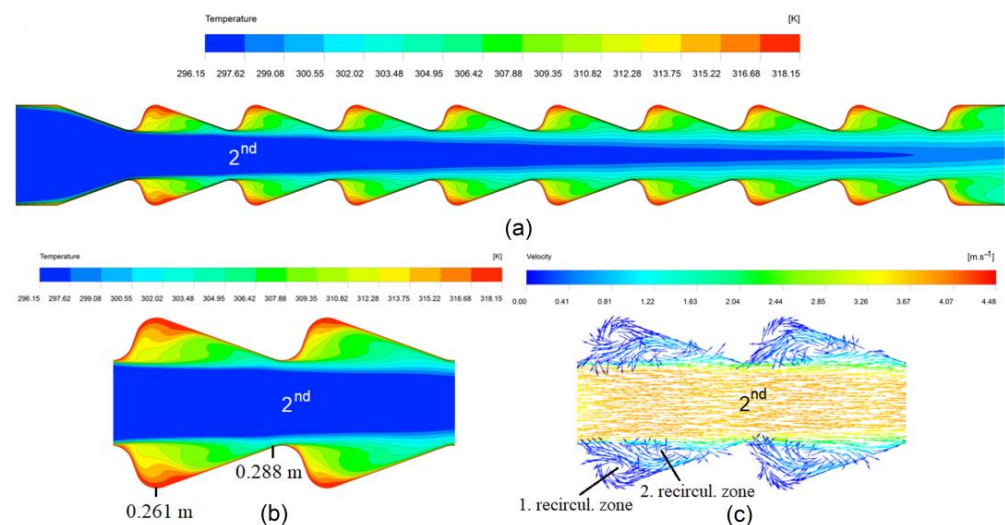

Figure 6. The temperature fields and velocity vectors of the WCA configuration ($Q = 50$ m^3/h), (**a**) temperature fields along the channel, (**b**) detail of the 2nd protrusion—temperature fields, (**c**) detail of the 2nd protrusion—velocity vectors.
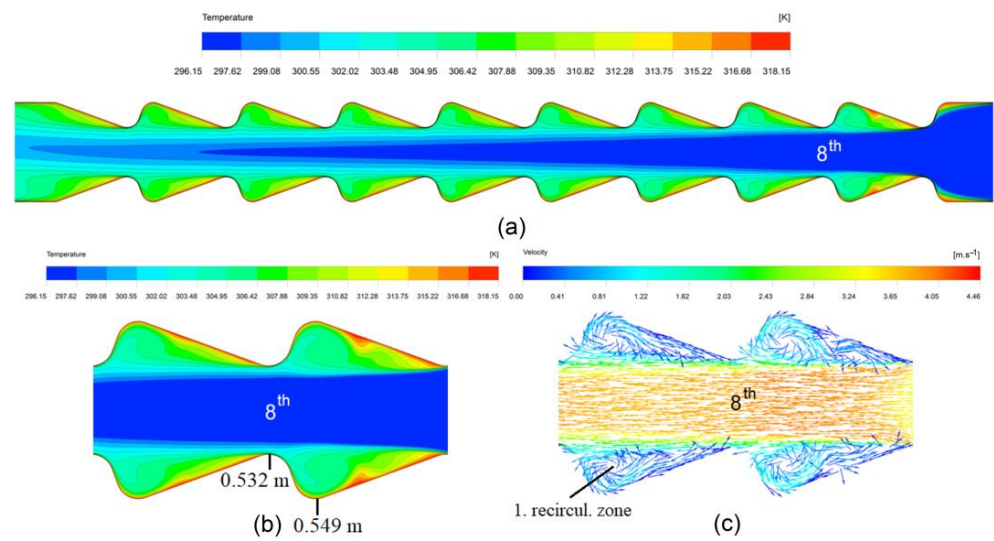
Figure 7. The temperature fields and velocity vectors of the WCB configuration (Q = 50 m^3/h), (**a**) temperature fields along the channel, (**b**) detail of the 8th protrusion—temperature fields, (**c**) detail of the 8th protrusion—velocity vectors.
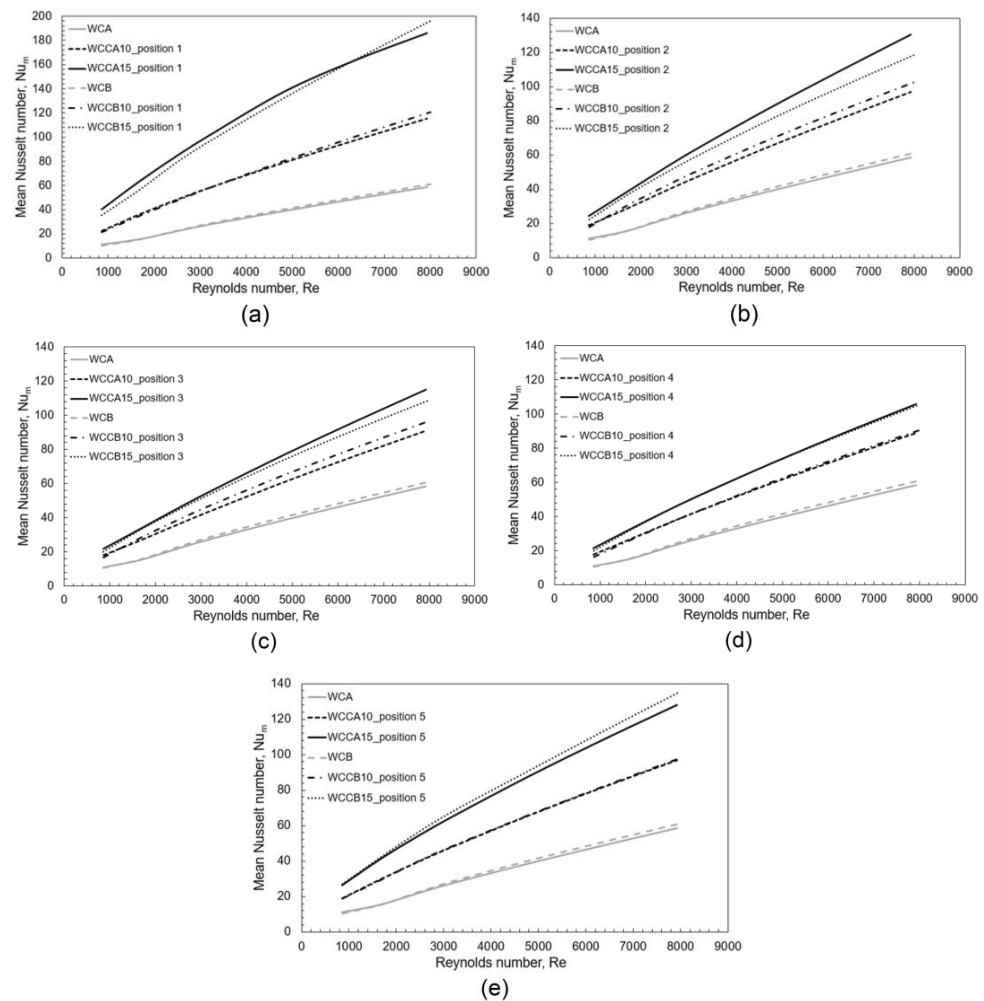

Figure 8. The effect of configuration and position of CVGs on the mean Nusselt number when changing the Reynolds number, (**a**) WC vs. WCC at the position '1', (**b**) WC vs. WCC at the position '2', (**c**) WC vs. WCC at the position '3', (**d**) WC vs. WCC at the position '4', (**e**) WC vs. WCC at the position '5'.

When investigating the CVGs diameter effect, the CVGs of 15 mm diameter achieved higher Nu_m values compared with 10 mm for all investigated positions (Figure 8). The Nu_m of the WCCA15 configuration is higher by 61.48% compared with the WCCA10 while the value for the WCCB15 is higher by 62.24% compared with the WCCB10 for position '1' and the flow rate of 50 m^3/h (Figure 8a). At position '4' (Figure 8d), there is a decrease in differences between the CVGs of 10 and 15 mm where the WCCA15 achieved higher values only by 18.76% compared with the WCCA10, while the WCCB15 obtained higher values only by 16.68% compared with the WCCB10. Air flow direction (inlet air A, B) does not significantly affect the change of Nu_m. The differences between Nu_m for the WCCA10–WCCB10 and WCCA15–WCCB15 represent the value of 5.69 and 10.10 for the position '1' and maximum flow rate of 50 m^3/h (Figure 8a). The positions '4' and '5' achieved differences ΔNu_m = 1.41 and 1.26 (Figure 8d,e).

The highest values of Nu_m were achieved for the configuration WCCA15, flow rate 5–30 m^3/h, and CVGs position '1' together with the configuration WCCB15, flow rate 40–50 m^3/h, and CVGs position '1' (Figure 8a). The comparison of h_x along lower and upper surfaces of the WCCA15 (Q = 5 m^3/h and 30 m^3/h) and WCCB15 (Q = 50 m^3/h) configurations for CVGs position '1' is shown in Figure 9. Based on the distribution of h_x values along the WCCB15 configuration, it can be clearly observed the increase of h_x peaks from the 3rd to 9th protrusions for the lower and upper surfaces. When increasing the flow rate Q, higher h_x values were achieved. With an increase in the flow rate, the thermal boundary layer is pressed against the heated surface and becomes thinner, and thus the heat transfer is improved. Higher air flow velocities also lead to more intense swirls in the valleys. From the distribution of h_x peaks of the WCCA15 (Q = 5 m^3/h and 30 m^3/h) is clearly observed the decrease along the channels. On the contrary, an increase of h_x peaks along the channel can be observed for backward air flow (WCCB15).
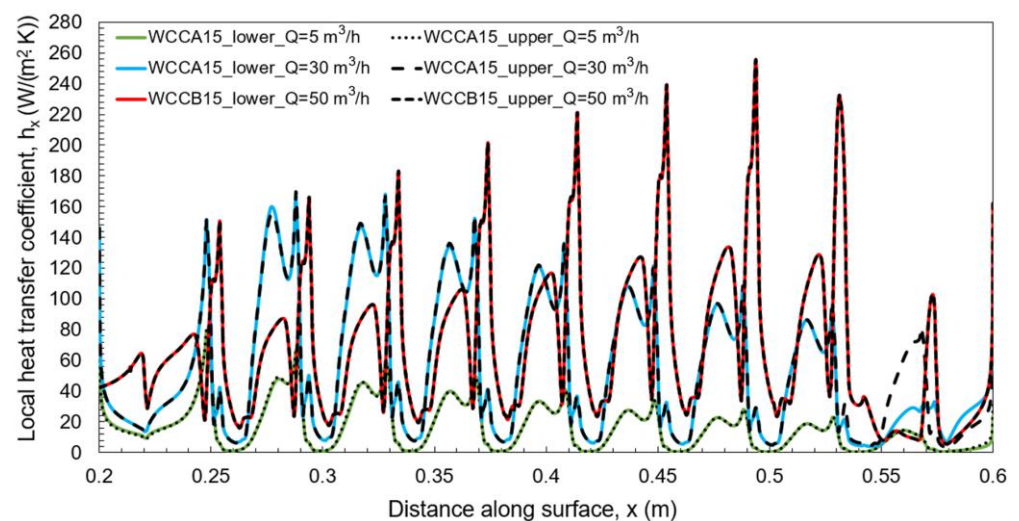

Figure 9. The comparison of the local heat transfer coefficients along lower and upper surfaces of the WCCA15 and WCCB15 configurations for CVGs position '1' when changing the flow rate.

The distributions of temperature fields and velocity vectors along the WCCB15 length for Re = 8001 (Q = 50 m^3/h) are shown in Figure 10. The CVGs position '1' caused maximum h_x values along the channel due to the efficient distribution of cooling air into the valleys (Figure 10a). The CVGs position '1' causes a significant compression of the thermal boundary layer, especially in front of the fifth to eighth peak of the protrusions, and a significant recirculation of air behind the CVGs, which leads to an important intensification of heat transfer. In the protrusion valleys, two recirculation zones are formed where higher air velocity improved the heat transfer (Figure 10b).
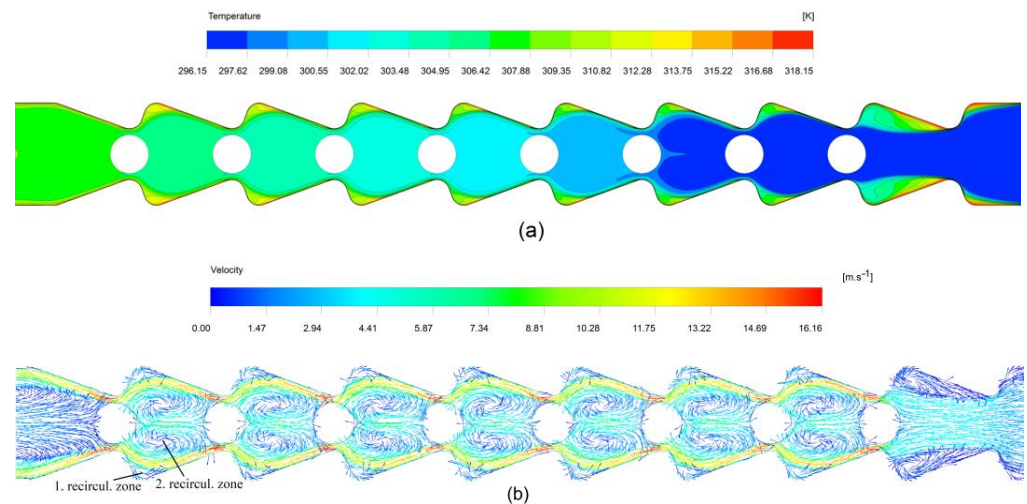
Figure 10. The temperature fields and velocity vectors of the WCCB15 for Q = 50 m^3/h and CVGs position '1', (**a**) temperature fields along the channel, (**b**) velocity vectors along the channel.

To assess the overall effectiveness of the examined wavy channels with/without CVGs, it is necessary to consider not only heat transfer parameters, but pressure drops as well. Generally, convective heat transfer and pressure drops are considered together to design the corrugated channels. On the basis of Equations (4) and (5), the Colburn factors j and friction factors f were calculated and their dependence on the Re is shown in Figure 11. The Colburn factor j is a dimensionless heat transfer parameter to represent the convection movement of heat. It decreases with Re for all investigated configurations. The maximum j was achieved for the WCCA15 configuration at CVGs position '1' and Re = 857 (j = 0.05208). With an increase of Re to 7927, the value of j decreased to 0.02604 (Figure 11a). At the same time, the friction factor f achieved the maximum value of 54.673 for the WCCA15 (CVGs position '1', Re = 857) and only slightly decreased with increased Re to 7927 (f = 50.511). The Colburn factor j decreased with CVGs position and for the position '5' it achieved the value j = 0.03414 for Re = 857.

The WCCA15 (position '1') reached 3.64 and 3.84 times higher values of j compared with the WCA and WCB configurations for Re = 857, respectively. The differences in j between the mentioned channels decreased with increased Re. Simultaneously, the friction factor f of the WCA and WCB configurations achieved the minimum values in the range of 0.483 to 0.514 for the WCA and 0.466 to 0.527 for the WCB depending on Re. When changing the CVGs position, the j values decreased to the position '4'; however, they increased at the position '5' for the whole range of Re. The values of f were significantly affected by the CVGs position (Figure 11f–j). For the WCCA15 configuration, CVGs at the position '2' caused a drop in f values in the range of 79.71% to 77.49% compared with the position '1'. A drop in f values in the range of 31.29% to 29.45% and 3.42% to 17.7% was noticed for the position '3' and '4', respectively. On the contrary, the position '5' caused an increase above the f values of the position '2' to '4', whereas the values were lower in the range of 68.99% to 72.42% compared with the position '1'.

From the standpoint of CVGs diameter, higher values of j together with f were achieved for the diameter of 15 mm compared with 10 mm for all investigated positions and Re. The WCCA15 and WCCB15 configurations showed higher j in the range of 80.58% to 61.54% and 66.15% to 62.19% compared with the WCCA10 and WCCB10 for CVGs position '1' and all Re. When changing the CVGs position ('1' to '4'), the differences between the mentioned configurations decreased. For the position '5', the different j values between the configurations with 15 mm and 10 mm CVGs diameter increased. Due to the CVGs diameter, lower values of the friction factor f were achieved for the WCCA10 and WCCB10 configurations compared with the WCCA15 and WCCB15, respectively. The WCCA15 and WCCB15 configurations showed higher f in the range of 5.75 to 5.68 times

and 5.05 to 3.94 times compared with the WCCA10 and WCCB10 for CVGs position '1' and all *Re*. The differences between the mentioned configurations decreased for the position '2' to '4', while an increase in the *f* value difference was achieved for the position '5'.
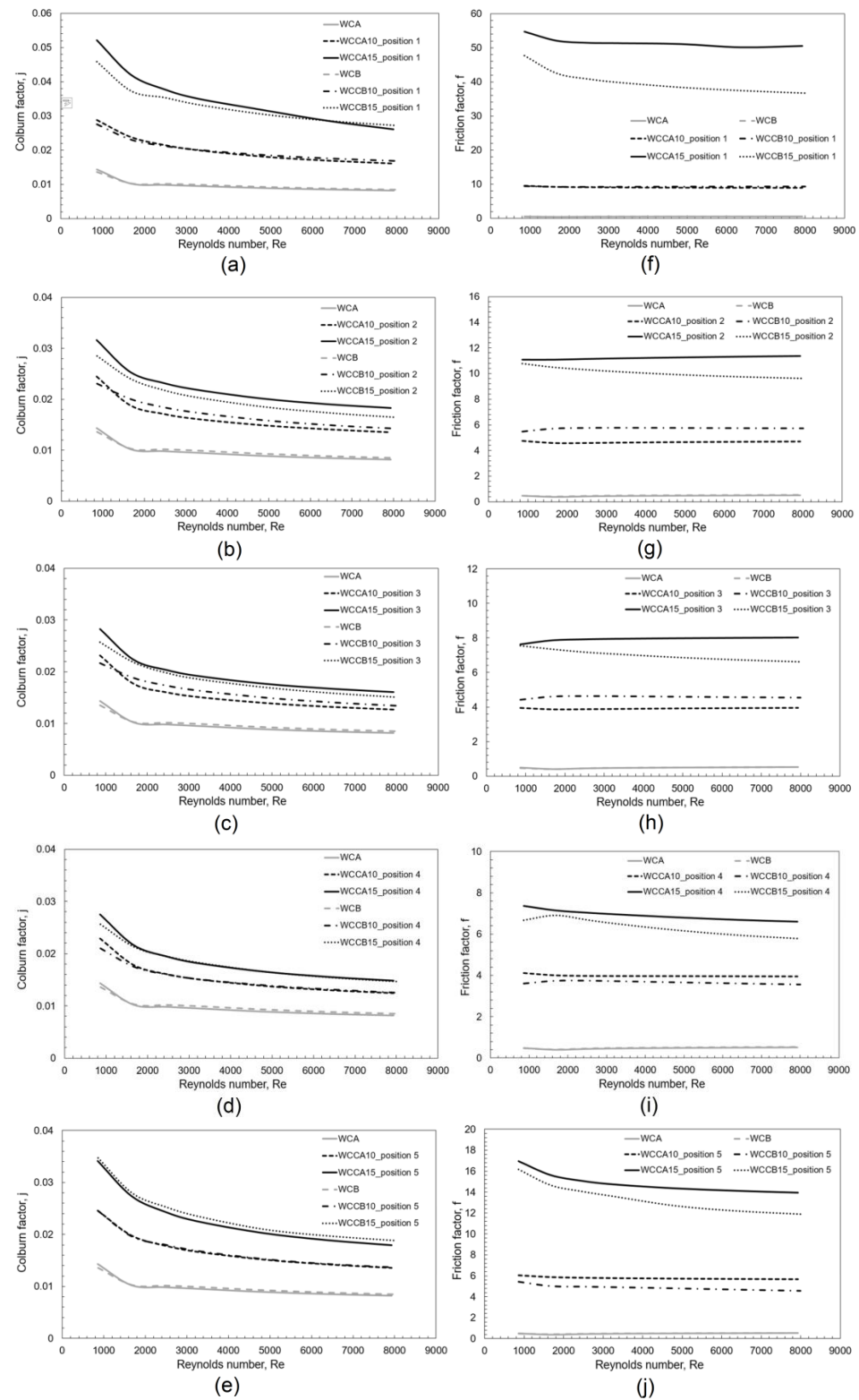

Figure 11. The effect of configuration and position of CVGs on the values of Colburn factor and Friction factor when changing Reynolds number, (**a**–**e**) WC vs. WCC at the position '1' to '5' in terms of Colburn factor, (**f**–**j**) WC vs. WCC at the position '1' to '5' in terms of Friction factor.

The comparison of h_x values for lower surfaces of the WCCA15 and WCCB15 configuration with CVGs position '1' to '5' and $Re = 857$ ($Q = 5$ m^3/h) is shown in Figures 12 and 13. Due to the change in the direction of the air flow (forward and backward), different h_x distributions along lower surfaces were achieved. While the peaks of the protrusions have a decreasing course with the channel length for the WCCA15 configuration, the WCCB15 has the opposite character. The maximum value of $h_x = 79.70$ W/(m^2·K) was noticed on the 1st peak for the position '1'. The positions '2' to '3' showed the decreasing course along the channel. The position '5' achieved maximum $h_x = 30.14$ W/(m^2·K) on the 3rd peak and gradually decreased (Figure 12). The maximum value of $h_x = 77.72$ W/(m^2·K) was noticed on the 8th peak of the WCCB15, while the 9th peak had a decreasing course for the position '1' (Figure 13). For the position '2' (WCCB15), there is a decreasing trend of peaks along the channel. The position '3' shows an increasing trend to the 6th peak with a subsequent decrease. The position '4' and '5' shows an increasing trend along the whole channel.
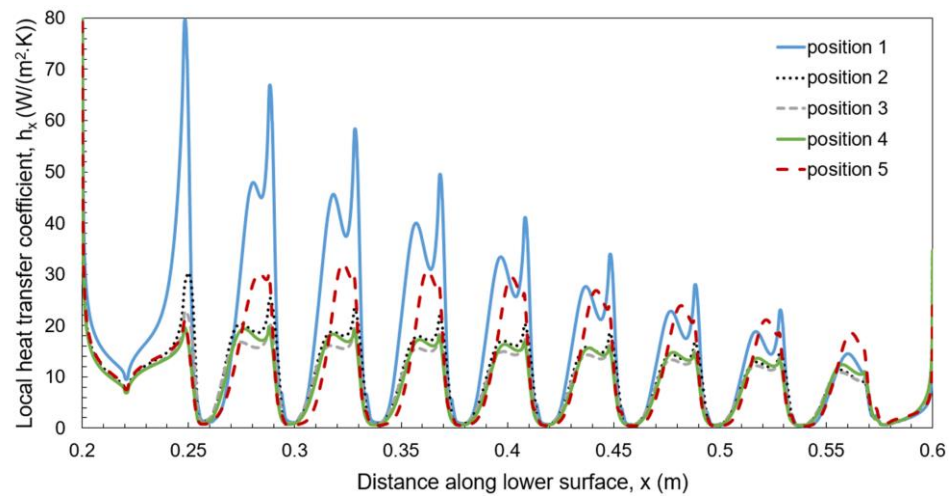

Figure 12. The comparison of local heat transfer coefficients along lower surfaces of the WCCA15 for CVGs position '1' to '5' and $Re = 857$.
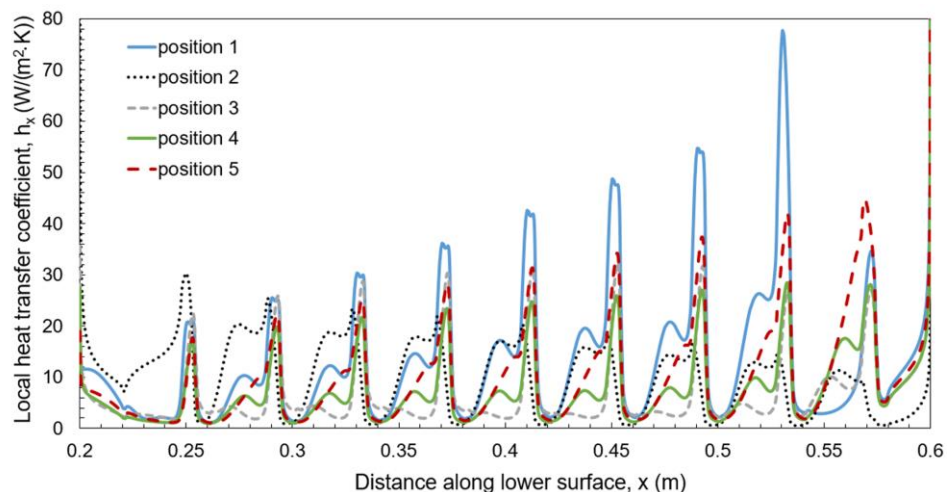

Figure 13. The comparison of local heat transfer coefficients along lower surfaces of the WCCB15 for CVGs position '1' to '5' and $Re = 857$.

The distributions of temperature fields and velocity vectors along the channel of the WCCA15 configuration for $Re = 857$ ($Q = 5$ m^3/h) and CVGs position '1' is shown in Figure 14. On the basis of the temperature fields (Figure 14a), it is clear that maximum h_x was achieved on the leading edge of the first protrusion (CVGs position '1') at the local

section 0.248 m. The low air velocity caused an accumulation of heat in the valleys and at the same time the CVGs position '1' caused an accumulation of heat behind them. Nevertheless, the position '1' caused better pressing of the thermal boundary layer compared with the other positions and it is the most effective in terms of the Colburn factor *j*. Three recirculation zones are formed in the valleys that enhanced the fluid mixing (Figure 14b). The distributions of temperature fields and velocity vectors along the channel of the WCCB15 configuration for *Re* = 857 (*Q* = 5 m^3/h) and CVGs position '1' is shown in Figure 15. Due to the backward air flow, maximum h_x is achieved on the 8th protrusion at the local section 0.530 m where the highest pressure of the thermal boundary layer to the wavy surface occurs. Two recirculation zones are formed in the individual valleys for lower and upper wavy surface (Figure 15b).
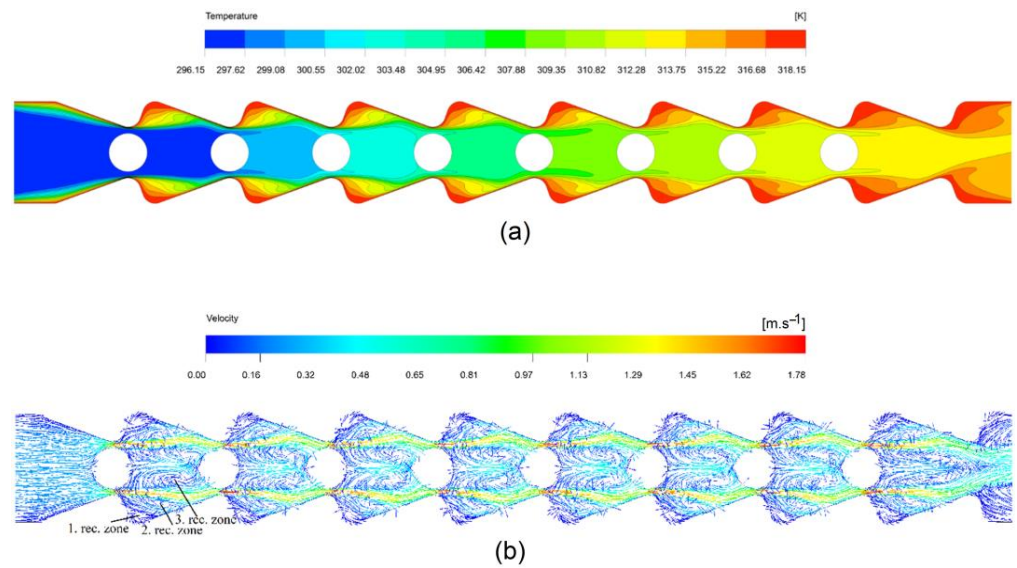

Figure 14. The temperature fields and velocity vectors of the WCCA15 (position '1') for *Re* = 857 (*Q* = 5 m^3/h), (**a**) temperature fields along the channel, (**b**) velocity vectors along the channel.

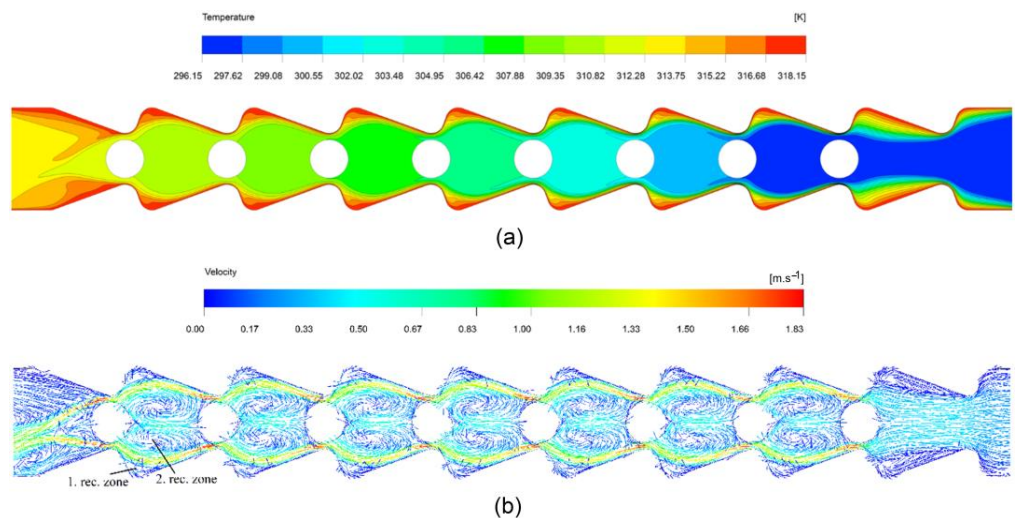**Figure 15.** The temperature fields and velocity vectors of the WCCB15 (position '1') for *Re* = 857 (*Q* = 5 m^3/h), (**a**) temperature fields along the channel, (**b**) velocity vectors along the channel.

The thermal performance factor for forward and backward air flow were calculated by Equations (6) and (7). The distributions of thermal performance factor TPF_A for the air inlet A and CVGs diameter of 10 mm and 15 mm are shown depending on *Re* in Figure 16a,b. When considering heat transfer parameters of the investigated configurations together with

pressure drops, the maximum TPF_A values in the range of 0.8170 to 0.7999 were achieved for the WCCA15 and the position '2' with Re = 1669–7930 (Figure 16b). For Re = 858 (Q = 5 m^3/h), the second highest value (TPF_A = 0.7769) was reached. For the WCCA10 and Re in the range of 2467 to 7930, the CVGs position '2' is efficient, while the position '1' and '3' are more appropriate for Re = 1669 (TPF_A = 0.8199) and Re = 858 (TPF_A = 0.8040), respectively.
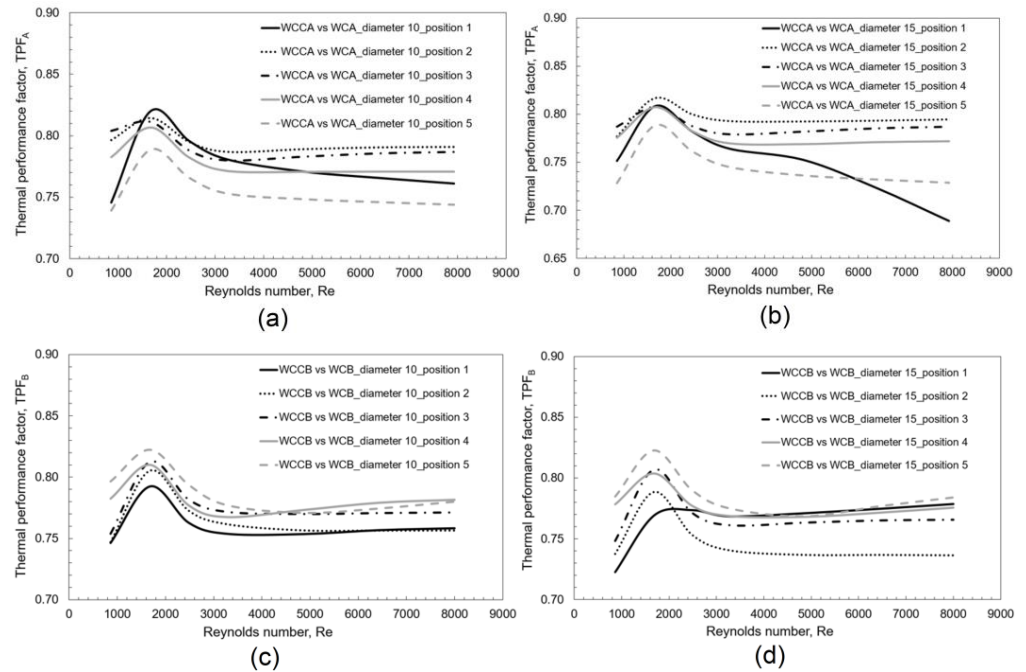

Figure 16. Thermal performance factor for different diameter and CVGs position 1–5, (**a**) WCCA vs. WCA for diameter of 10 mm, (**b**) WCCA vs. WCA for diameter of 15 mm, (**c**) WCCB vs. WCB for diameter of 10 mm, (**d**) WCCB vs. WCB for diameter of 15 mm.

The distributions of thermal performance factor TPF_B for the air inlet B depending on Re is shown in Figure 16c,d for 10 and 15 mm diameter. The maximum TPF_B values in the range of 0.8229 to 0.7684 were achieved for the WCCB15 and the position '5' in the range of Re = 861 to 3279 and 6432 to 7989 (Figure 16d). For 10 mm diameter, the maximum TPF_B values in the range of 0.7769 to 0.8222 (Re = 862 to 3282) were achieved for the WCCB10 configuration and the position '5' (Figure 16c). The WCCB10 configuration and the position '4' is more efficient one for Re in the range of 4869 to 7999 where TPF_B = 0.7733–0.7816. The maximum thermal performance factor TPF_B = 0.8229 was noticed for the WCCB15, CVGs position '5' and Re = 1677 (Q = 10 m^3/h). The temperature field, pressure field, and velocity vectors are shown in Figure 17.

The highest thermal performance factor was achieved for the configuration WCCB15 and Q = 10 m^3/h at CVGs position '5'. The temperature field (Figure 17a) shows that the backward air flow is effective since the cooling air gets to a greater extent into the valleys and thus better fluid mixing occurs. At the same time, CVGs position '5' is also effective in terms of pressure drops in this flow direction. Two recirculation zones are formed in the valleys of individual protrusions (Figure 17b). The CVGs significantly help to compress the thermal boundary layer to the wavy surface and to direct the flowing air into the protrusion valleys. From the distribution of pressure fields along the channel of WCCA15 configuration (Figure 17c), it can be observed that total pressure increase with the channel length. A higher total pressure occurs in the valleys compared with the area behind the CVGs. Due to the CVGs' location close to the top of the protrusions, a greater compression of the cooling air into the valleys appears there; consequently, the air must overcome greater resistance when passing through the next protrusions. The distribution of the turbulence kinetic energy is shown in Figure 17d. The maximum turbulence kinetic

energy in the range of 0.148 to 0.181 m^2/s^2 is found on the leading side of '3'–'8' CVGs and between the 9th protrusions. The CVGs location behind each other and narrowed space between the protrusion peaks caused an increase in the turbulence kinetic energy.
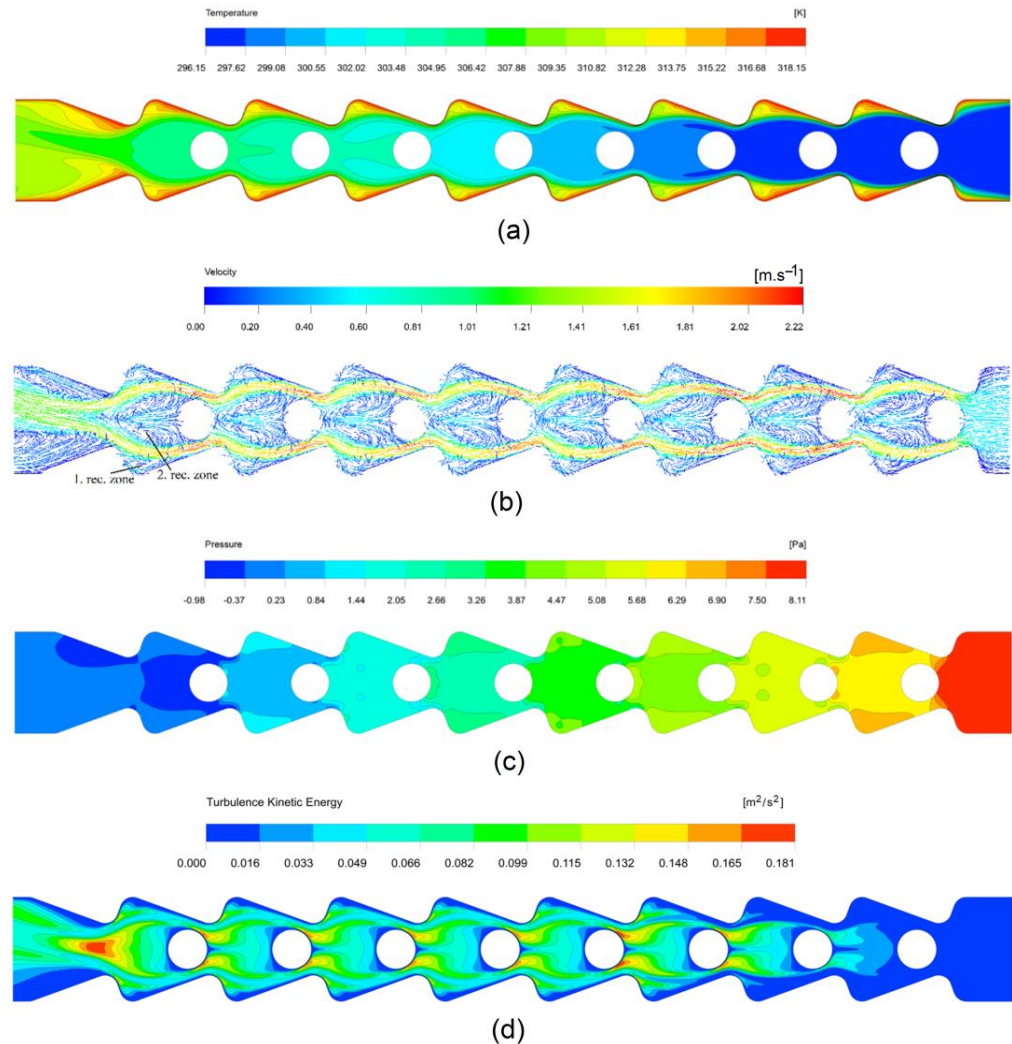

Figure 17. WCCB15 configuration for CVGs position '5' for *Re* = 1677 (*Q* = 10 m3/h), (**a**) temperature field, (**b**) velocity vectors, (**c**) pressure field, (**d**) turbulence kinetic energy.

The distribution of x-velocities for the WCCB15 configuration (CVGs position '5') for *Q* = 10 m^3/h is shown in Figure 18. The values of x-velocities for the 1st to 8th valley are shown at the local sections from 0.26 m to 0.54 m with the spacing 0.04 m (Figure 18a) and for the 1st to 9th peak at the local sections from 0.25 m to 0.57 m with the same spacing (Figure 18b). The distribution of x-velocities at the local sections of the valleys V1 to V8 acquired a similar character in the range of 0.535 m/s to −1.945 m/s. The local sections in the valleys V7 and V6 achieved the maximum velocity of −1.945 m/s and −1.799 m/s in y-position of −0.011 m. The cooling air (in backflow) hits the CVG directly and surrounds it, while thanks to the narrow gap between the CVG and the protrusion, the effect of intense air pressure on the protrusion is created, which also has a positive effect on behavior in valleys. In the middle of the wavy channel (y-position of 0 m), x-velocities in the range of 0.439 m/s to 0.535 m/s were achieved. Gradually with the increase of y-position, the x-velocities increased to negative values (backflow) to y-position of 0.011 m (respectively −0.011 m) and subsequently the velocity decreased again and reached the 0 m/s in y-position of 0.016 m (respectively −0.016 m). The distribution of x-velocities at the local sections of the peaks P2 to P8 acquired a similar character; the peaks P1 and P9 were

affected by the inlet and outlet section of the channel. In the middle of the wavy channel between the peaks of protrusions, the minimum x-velocities approaching 0 m/s were achieved. Gradually with the increase of y-position, the x-velocities increased to velocities 0.238 m/s and subsequently to −2.174 m/s in y-position of 0.009 m (respectively −0.009 m) and decreased towards 0 m/s again. The maximum x-velocities achieved in y-position of 0.009 m is the result of air pressing and at the same time also pressing of the thermal boundary layer.
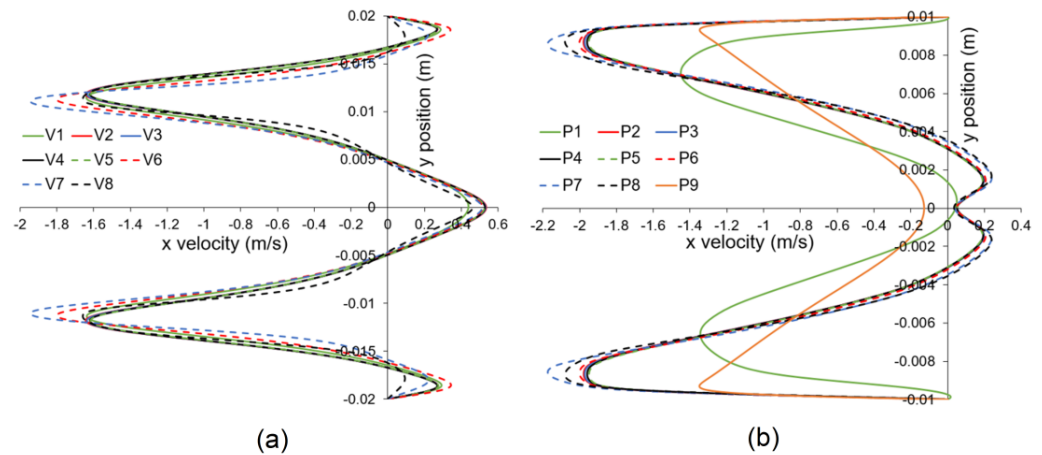

Figure 18. Distribution of x-velocities of the WCCB15 configuration for CVGs position '5' for *Re* = 1677 (*Q* = 10 m³/h), (**a**) sections of the 1st to 8th valley, (**b**) sections of the 1st to 9th peak.

New correlating equations for the mean Nusselt number Nu_m were created for the WCCA and WCCB configurations and CVGs position of '1' to '5' for the flow rate Q in the range of 10 m³/h to 50 m³/h, CVGs diameter of D = 10 mm and 15 mm, and the channel height H = 40 mm.

WCCA15 configuration (CVGs position '1' to '5'):

$$
\begin{aligned}
Nu_m &= Re^{-0.494(D/H)+0.872} \cdot (D/H)^{-3.860(D/H)+2.390} \\
Nu_m &= Re^{-0.017(D/H)+0.801} \cdot (D/H)^{3.567(D/H)+0.970} \\
Nu_m &= Re^{-0.001(D/H)+0.798} \cdot (D/H)^{4.396(D/H)+0.817} \\
Nu_m &= Re^{-0.115(D/H)+0.808} \cdot (D/H)^{3.533(D/H)+0.926} \\
Nu_m &= Re^{-0.224(D/H)+0.819} \cdot (D/H)^{1.124(D/H)+1.363}
\end{aligned}
\tag{18}
$$

with the percent standard deviation of the error E_{SD} = 0.77%, and the error E ranged from −2.34% to +2.69%.

WCCB15 configuration (CVGs position '1' to '5'):

$$
\begin{aligned}
Nu_m &= Re^{-0.129(D/H)+0.831} \cdot (D/H)^{0.559(D/H)+1.583} \\
Nu_m &= Re^{-0.156(D/H)+0.820} \cdot (D/H)^{3.078(D/H)+0.953} \\
Nu_m &= Re^{-0.120(D/H)+0.814} \cdot (D/H)^{3.844(D/H)+0.824} \\
Nu_m &= Re^{-0.269(D/H)+0.859} \cdot (D/H)^{2.511(D/H)+1.255} \\
Nu_m &= Re^{-0.139(D/H)+0.801} \cdot (D/H)^{1.592(D/H)+1.259}
\end{aligned}
\tag{19}
$$

with the percent standard deviation of the error E_{SD} = 0.52%, and the error E ranged from −1.06% to +2.18%. The correctness of the correlating equations is shown in Figure 19 where the values of Nu_m from the correlating equations and numerical simulations were compared.
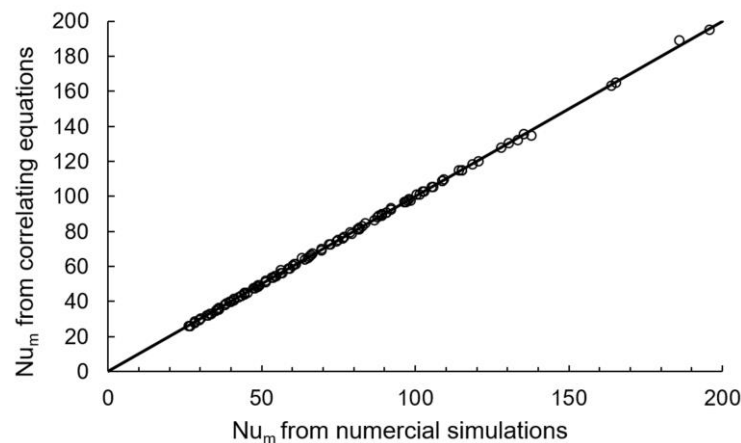
Figure 19. Comparison between new correlating equations and numerical results.

5. Conclusions

Today, it is necessary to put even more emphasis on saving energy and efficient heat transfer in heat exchanger types. The improvement in heat transfer characteristics was achieved by the novel asymmetric wavy geometry of the heated channel. Inserting the CVGs to the channel led to directing and pressing of cooling air into the valleys and to better air recirculation. On the basis of this, there was the enhancement of Nusselt numbers and Colburn factors for all positions of CVGs and *Re* compared with the channels without CVGs. The backward flow of cooling air brought an improvement in terms of thermal-hydraulic characteristics compared with the forward flow.

The configuration of wavy channel with CVGs of 15 mm at the position '5' for *Re* = 1677 and backward flow air is the most effective in terms of heat transfer and pressure drops. The new correlating equations for the mean Nusselt number Nu_m were created for the WCCA and WCCB configurations for CVGs position '1' to '5', flow rate in the range of 10 m³/h to 50 m³/h, CVGs diameter of 10 mm and 15 mm, and the channel height 40 mm.

The specifically following conclusions can be made from the current study:

1. The experimentally and numerically obtained local heat transfer coefficients h_{xexp} and h_{num} are in good agreement for the WCA and WCCA15 configurations for the channel height 40 mm and flow rate in the range of 5 to 20 m³/h.

2. In terms of comparing the wavy channels without CVGs:
   - The Nu_m increased with *Re* for all investigated configurations.
   - The Nu_m for the WCB were higher in the range of 1.28% to 5.09% compared with the WCA for Q = 10 to 50 m³/h. On the contrary, the WCA for Q = 5 m³/h achieved higher Nu_m by 4.78% with to the WCB.
   - The backward air flow improved the local and mean heat transfer parameters compared with the forward one. The cooling air causes better mixing in valleys for the WCB configuration, which leads to more efficient heat transfer in the valleys and subsequently to higher h_x compared with the WCA configuration.

3. In terms of comparing the wavy channels with CVGs:
   - The wavy channels with CVGs achieved the higher Nu_m for all investigated positions compared with the WCA and WCB configurations. The Nu_m increased 3.35 times for the WCCA15 (position '1') compared with the WCA for maximum flow rate of 50 m³/h.
   - The values of Nu_m decreases with CVGs position ('1' to '4'); however, there is an increase at the position '5'.
   - The maximum Nu_m in the range of 40.21 to 163.74 (*Re* = 857 to 6383) was achieved for the configuration of the WCCA15 and CVGs position '1'; the maximum

Nu_m = 196.00 was achieved for the configuration of WCCB15 (position '1') for Re = 8000.

- The CVGs of 15 mm diameter achieved higher Nu_m compared with 10 mm for all investigated positions. The Nu_m of the WCCA15 configuration is higher by 61.48% compared with the WCCA10, while the WCCB15 configuration is higher by 62.24% compared with the WCCB10 for the position '1' and flow rate of 50 m^3/h.

- The differences between Nu_m of the WCCA10 – WCCB10 and WCCA15–WCCB15 for the position '1' and flow rate of 50 m^3/h represent the value 5.69 and 10.10, respectively. The highest values of Nu_m were achieved for the configuration WCCA15 for flow rate 5 to 30 m^3/h, position '1' and the configuration WCCB15 for flow rate 40 to 50 m^3/h, position '1'.

- The Colburn factor j decreased with Re for all investigated configurations. The value of j = 0.05208 achieved the maximum for the WCCA15, position '1' and Re = 857. The mentioned configuration reached 3.64 and 3.84 times higher values of j compared with the WCA and WCB. The values of j, f were significantly affected by the position and diameter of CVGs. The WCCA15 (position '2') caused a drop in f values up to the 79.71% compared with the position '1'. The diameter of 15 mm caused higher j and f values for all Re compared with 10 mm.

- The maximum TPF_A in the range of 0.8170 to 0.7999 were achieved for the WCCA15, position '2' and Re = 1669–7930. The maximum TPF_B in the range of 0.8229 to 0.7684 were achieved for the WCCB15, position '5' and Re = 861–3279 and 6432–7989. Specifically, TPF_B = 0.8229 was achieved the WCCB15, position '5' and Re = 1677 (Q = 10 m^3/h).

The conclusions of the presented work can be the basis for further research, e.g., other surface temperatures, cooling air temperatures, channel height, spacing of protrusions, inline and offset protrusions configuration, and shape and position of CVGs in the channel.

Author Contributions: Conceptualization, Z.B.; methodology, S.K.; software, S.K.; validation, Z.B.; formal analysis, S.K.; investigation, Z.B.; resources, Z.B.; data curation, S.K.; writing—original draft preparation, Z.B.; writing—review and editing, S.K.; visualization, S.K.; supervision, Z.B.; project administration, Z.B.; funding acquisition, S.K. All authors have read and agreed to the published version of the manuscript.

Data Availability Statement: Not applicable.

Nomenclature

Roman Symbols:

c_p	specific heat capacity at constant pressure, J/(kg·K)
D	outer diameter of vortex generator, m
D_{hyd}	hydraulic diameter, m
f	friction factor
g	gravity vector
h	heat transfer coefficient, W/(m^2·K)
H	channel height, m
j	Colburn factor
k	thermal conductivity coefficient, W/(m·K)
L	contour length of wavy surfaces in the test section, m
L_2	length of the heated test section, m

Nu	Nusselt number
p	pressure of air, Pa
Pr	Prandtl number
q	heat flux, W/m^2
Q	flow rate, m^3/h
Re	Reynolds number
s	spacing, m
T	temperature, K
TPF	thermal performance factor
v	velocity of air, m/s
v	velocity vector
Greek Symbols:	
Δ	difference values
η	thermal performance
μ	dynamic viscosity, kg/(m·s)
ρ	density of air, kg/m^3
Subscripts:	
a	air
A	forward flow
B	backward flow
exp	experimental
in	inlet
l	lower
out	outlet
m	mean values
num	numerical
s	surface
u	upper
x	local value

References

1. Kolsi, L.; Selimefendigil, F.; Ghachem, K.; Alqahtani, T.; Algarni, S. Multiple Impinging Jet Cooling of a Wavy Surface by Using Double Porous Fins under Non-Uniform Magnetic Field. *Mathematics* **2022**, *10*, 638. [CrossRef]
2. Naphon, P. Heat transfer characteristics and pressure drop in channel with V corrugated upper and lower plates. *Energy Convers. Manag.* **2007**, *48*, 1516–1524. [CrossRef]
3. Naphon, P. Laminar convective heat transfer and pressure drop in the corrugated channels. *Int. Commun. Heat Mass Transf.* **2007**, *34*, 62–71. [CrossRef]
4. Singh, S.; Singh, A.; Chander, S. Thermal performance of a fully developed serpentine wavy channel solar air heater. *J. Energy Storage* **2019**, *25*, 100896. [CrossRef]
5. Bezbaruah, P.J.; Das, R.S.; Sarkar, B.K. Experimental and numerical analysis of solar air heater accoutered with modified conical vortex generators in a staggered fashion. *Renew. Energ.* **2021**, *180*, 109–131. [CrossRef]
6. Silva, F.A.S.; Dezan, D.J.; Pantaleão, A.V.; Salviano, L.O. Longitudinal vortex generator applied to heat transfer enhancement of a flat plate solar water heater. *Appl. Therm. Eng.* **2019**, *158*, 10. [CrossRef]
7. Zhao, Z.; Luo, L.; Qiu, D.; Wang, Z.; Sundén, B. On the solar air heater thermal enhancement and flow topology using differently shaped ribs combined with delta-winglet vortex generators. *Energy* **2021**, *224*, 17. [CrossRef]
8. Caliskan, S.; Şevik, S.; Özdilli, Ö. Heat transfer enhancement by a sinusoidal wavy plate having punched triangular vortex generators. *Int. J. Therm. Sci.* **2022**, *181*, 17. [CrossRef]
9. Nassab, S.A.G.; Sheikhnejad, Y.; Nia, M.F. Novel design of natural solar air heat for higher thermal performance utilizing porous vortex generator. *Therm. Sci. Eng. Prog.* **2022**, *33*, 11. [CrossRef]
10. Kurtulmus, N.; Zontul, H.; Sahin, B. Heat transfer and flow characteristics in a sinusoidally curved converging-diverging channel. *Int. J. Therm. Sci.* **2020**, *148*, 106163. [CrossRef]
11. Liu, C.; Teng, J.T.; Chu, J.C.; Chiu, Y.L.; Huang, S.; Jin, S.; Dang, T.; Greif, R.; Pan, H.H. Experimental investigations on liquid flow and heat transfer in rectangular microchannel with longitudinal vortex generators. *Int. J. Heat Mass Transf.* **2011**, *54*, 3069–3080. [CrossRef]
12. Chen, C.; Teng, J.T.; Cheng, C.H.; Jin, S.; Huang, S.; Liu, C.; Lee, M.T.; Pan, H.H.; Greif, R. A study on fluid flow and heat transfer in rectangular microchannels with various longitudinal vortex generators. *Int. J. Heat Mass Transf.* **2014**, *69*, 203–214. [CrossRef]
13. Ebrahimi, E.; Roohi, S.; Kheradmand, S. Numerical study of liquid flow and heat transfer in rectangular microchannel with longitudinal vortex generators. *Appl. Therm. Eng.* **2015**, *78*, 576–583. [CrossRef]

14. Raihan, M.F.B.; Al-Asadi, M.T.; Thompson, H.M. Management of conjugate heat transfer using various arrangements of cylindrical vortex generators in micro-channels. *Appl. Therm. Eng.* **2021**, *182*, 15. [CrossRef]

15. Moosavi, R.; Banihashemi, M.; Lin, C.X.; Abel Chuang, P.Y. Combined effects of a microchannel with porous media and transverse vortex generators (TVG) on convective heat transfer performance. *Int. J. Therm. Sci.* **2021**, *166*, 15. [CrossRef]

16. Amini, Y.; Habibi, S.E. Effects of multiple flexible vortex generators on the hydrothermal characteristics of a rectangular channel. *Int. J. Therm. Sci.* **2022**, *175*, 14. [CrossRef]

17. Al-Asadi, M.T.; Alkasmoul, F.S.; Wilson, M.C.T. Heat transfer enhancement in a micro-channel cooling system using cylindrical vortex generators. *Int. Commun. Heat Mass Transf.* **2016**, *74*, 40–47. [CrossRef]

18. Al-Asadi, M.T.; Alkasmoul, F.S.; Wilson, M.C.T. Benefits of spanwise gaps in cylindrical vortex generators for conjugate heat transfer enhancement in micro-channels. *Appl. Therm. Eng.* **2018**, *130*, 571–586. [CrossRef]

19. Leu, J.S.; Wu, Y.H.; Jang, J.Y. Heat transfer and fluid flow analysis in plate-fin and tube heat exchangers with a pair of block shape vortex generators. *Int. J. Heat Mass Transf.* **2004**, *47*, 4327–4338. [CrossRef]

20. Cheraghi, M.; Raisee, M.; Moghaddami, M. Effect of cylinder proximity to the wall on channel flow heat transfer enhancement. *Comptes Rendus Mécanique* **2014**, *342*, 63–72. [CrossRef]

21. Wang, J.; Zhao, Y. Heat and fluid flow characteristics of a rectangular channel with a small diameter circular cylinder as vortex generator. *Int. J. Therm. Sci.* **2015**, *92*, 1–13. [CrossRef]

22. Wang, J.; Wang, C. Heat transfer and flow characteristics of a rectangular channel with a small circular cylinder having slit-vent vortex generator. *Int. J. Therm. Sci.* **2016**, *104*, 158–171. [CrossRef]

23. Han, Z.; Xu, Z.; Wang, J. $CaSO_4$ fouling characteristics on the rectangular channel with half-cylinder vortex generators. *Appl. Therm. Eng.* **2018**, *128*, 1456–1463. [CrossRef]

24. Han, Z.; Xu, Z.; Qu, H. Parametric study of the particulate fouling characteristics of vortex generators in a heat exchanger. *Appl. Therm. Eng.* **2020**, *167*, 10. [CrossRef]

25. Vyas, A.; Mishra, B.; Agrawal, A.; Srivastava, A. Non-intrusive investigation of flow and heat transfer characteristics of a channel with a built-in circular cylinder. *Phys. Fluids* **2018**, *30*, 22. [CrossRef]

26. Dey, P. Optimal position of square cylinder vortex generator in channel is not a function of ordinate only—A heat transfer and optimization study. *Eng. Sci. Technol.* **2022**, *28*, 11. [CrossRef]

27. Wang, J.; Yu, K.; Ye, M.; Wang, E.; Wang, W.; Sundén, B. Effects of pin fins and vortex generators on thermal performance in a microchannel with Al2O3 nanofluids. *Energy* **2022**, *239*, 14. [CrossRef]

28. Wu, J.M.; Tao, W.Q. Effect of longitudinal vortex generator on heat transfer in rectangular channels. *Appl. Therm. Eng.* **2012**, *37*, 67–72. [CrossRef]

29. Zhang, G.; Liu, J.; Sundén, B.; Xie, G. Combined experimental and numerical studies on flow characteristic and heat transfer in ribbed channels with vortex generators of various types and arrangements. *Int. J. Therm. Sci.* **2021**, *167*, 14. [CrossRef]

30. Ibrahim, A.Q.; Alturaihi, R.S. Experimental work for single-phase and two-phase flow in duct banks with vortex generators. *Results Eng.* **2022**, *15*, 16. [CrossRef]

31. Sui, Y.; Teo, C.J.; Lee, P.S. Direct numerical simulation of fluid flow and heat transfer in periodic wavy channels with rectangular cross-sections. *Int. J. Heat Mass Transf.* **2012**, *55*, 73–88. [CrossRef]

32. Brodnianská, Z.; Kotšmíd, S. Intensification of convective heat transfer in new shaped wavy channel configurations. *Int. J. Therm. Sci.* **2021**, *162*, 17. [CrossRef]

33. Menni, Y.; Ameur, H.; Sharifpur, M.; Ahmadi, M.H. Effects of in-line deflectors on the overall performance of a channel heat exchanger. *Eng. Appl. Comput. Fluid Mech.* **2021**, *15*, 512–529. [CrossRef]

34. Islamoglu, Y.; Parmaksizoglu, C. The effect of channel height on the enhanced heat transfer characteristics in a corrugated heat exchanger channel. *Appl. Therm. Eng.* **2003**, *23*, 979–987. [CrossRef]

35. Elshafei, E.A.M.; Awad, M.M.; Negiry, E.; Ali, A.G. Heat transfer and pressure drop in corrugated channels. *Energy* **2010**, *35*, 101–110. [CrossRef]

36. Cernecky, J.; Koniar, J.; Brodnianska, Z. The effect of regulating elements on convective heat transfer along shaped heat exchange surfaces. *Chem. Process Eng.* **2013**, *34*, 5–16. [CrossRef]